Characteristics of Mountain-Induced Thunderstorms and Cumulus Congestus Clouds from Budget Measurements

DAVID J. RAYMOND AND MARVIN WILKENING

Physics Department and Geophysical Research Center, New Mexico Institute of Mining and Technology, Socorro, NM 87801

(Manuscript received 19 June 1984, in final form 6 December 1984)

ABSTRACT

Apparent mass, moisture and energy sources associated with individual cumulus congestus and thunderstorm clouds are measured using an instrumented aircraft. The results for thunderstorms are similar to those obtained by other investigators. Cumulus congestus clouds differ greatly from thunderstorms and show the important role of mixing in producing downdrafts. The thunderstorm profiles are strongly affected by precipitation-induced downdrafts.

1. Introduction

Budget residual techniques are a useful way of assessing the effect of cumulus convection on the large-scale flow. Up to now these techniques have been used on the synoptic scale (e.g., Yanai *et al.*, 1973) and the mesoscale (Fankhauser, 1969, 1974; Betts, 1973; Sanders and Paine, 1975; Ogura and Chen, 1977; McNab and Betts, 1978).

We report here the use of an instrumented aircraft to obtain budget residuals on individual convective clouds. These measurements are an outgrowth of earlier convergence box techniques described by Raymond and Wilkening (1980, 1982). The National Center for Atmospheric Research (NCAR) Sabreliner was used rather than the previously employed Queen Air in order to obtain measurements more rapidly and over a greater range in altitude.

In this paper we are able to examine the difference between (for the most part) nonprecipitating cumulus congestus clouds and active thunderstorms. Our results on thunderstorms are similar to those obtained by other investigators, most notably Fankhauser (1969) and McNab and Betts (1978). However, the cumulus congestus clouds exhibited significantly different profiles of residuals, which must be attributed to the absence of precipitation and associated downdrafts.

Section 2 of this paper develops the diagnostic scheme employed here. The observations are described in Section 3, and the results are presented in Section 4. The significance of these observations is discussed in Section 5.

2. Budget model

As an example of a budget calculation we analyze the moisture budget. The governing equation for moisture is

$$\frac{dq}{dt} = -C, \tag{1}$$

where C is the net condensation rate and q the water vapor mixing ratio. We make a division of q into ambient and perturbation parts, $q = Q + q'$. Expanding in terms of pressure coordinates, (1) may be written

$$\frac{\partial q}{\partial t} + \mathbf{v}\cdot\nabla Q + \nabla\cdot(\mathbf{v}q') + \omega\frac{\partial Q}{\partial p} = -C - \frac{\partial(\omega q')}{\partial p} \equiv S_q, \tag{2}$$

where use has been made of the continuity equation

$$\nabla\cdot\mathbf{v} + \frac{\partial\omega}{\partial p} = 0. \tag{3}$$

The variables $\mathbf{v}$ and ω are respectively the horizontal velocity and the vertical pressure velocity. The isobaric gradient is ∇ and p is the pressure. The symbol S_q is called the *apparent moisture source.* The apparent moisture source contains contributions from condensation and evaporation as well as vertical eddy transports. Above the boundary layer both are likely to be confined to cloudy regions.

Subject to certain caveats, S_q integrated over the area of a single cloud may be obtained without entering the cloud. Indicating an areal integral over a cloud at constant pressure by a caret, (2) becomes

$$\frac{\partial\hat{q}}{\partial t} + F_q + \hat{\omega}\frac{\partial Q}{\partial p} = \hat{S}_q \tag{4}$$

upon integration.

The *detrained moisture flux* F_q arises from the advection term and the pure translation part of the time derivative, and is defined

$$F_q = \oint q'(\mathbf{v} - \mathbf{V}_t)\cdot \mathbf{n} dl, \tag{5}$$

where $\mathbf{V}_t$ is the translation velocity of the cloud, or more precisely, the translation velocity of the associated integration area. The line integral is around the periphery of the integration area, and $\mathbf{n}$ is the unit horizontal outward normal.

Equation (5) can be evaluated by measurements on the periphery of a cloud as long as Q is known. The quantity $\hat{\omega}$ in the third term in (4) is just the vertical mass flux, and this can similarly be evaluated using (3):

$$\hat{\omega} = -\int dp \oint \mathbf{v}\cdot\mathbf{n} dl \equiv -\int F dp. \tag{6}$$

The *detrained mass flux* is F, while the *vertical mass flux* is $\hat{\omega}$. Only the first term in (4) requires direct measurements inside the cloud and in a steady situation this term vanishes.

The evaluation of the line integral in (5) requires that Q be defined. This is because q rather than $q' = q - Q$ is actually measured. Though the division into ambient and perturbation parts is arbitrary, a consistent definition must be followed throughout the analysis. For the purposes of this paper we let Q be the average value of q along the aircraft track around the cloud at that level.

Equations analogous to (2), (4) and (5) can be immediately written down for the potential and equivalent potential temperatures θ and θ_e. The equivalent potential temperature is particularly interesting because (ignoring radiation) it is conserved in clouds. The apparent equivalent potential temperature source is thus, in analogy with (2),

$$S_e = -\frac{\partial(\omega\theta'_e)}{\partial p}. \tag{7}$$

Integration in pressure and over the area of the cloud yields

$$\int_{p_t}^{p_s} \hat{S}_e dp = -\int (\omega\theta'_e)|_{p=p_s} dA, \tag{8}$$

where the equivalent potential temperature flux is assumed zero at cloud top $p = p_t$, and p_s is the surface pressure. The mean surface heat flux (sensible + latent) H can be related to $(\omega\theta'_e)$ if the cloud area A_c is known:

$$H = -\frac{C_p\langle T\rangle}{gA_c\langle\theta_e\rangle}\int (\omega\theta'_e)|_{p=p_s} dA$$

$$= \frac{C_p\langle T\rangle}{gA_c\langle\theta_e\rangle}\int_{p_t}^{p_s} \hat{S}_e dp. \tag{9}$$

The surface latent heat flux directly under a cloud probably contributes negligibly to the moisture budget of the cloud. This hypothesis can be tested by integrating (2) in the same manner:

$$\int_{p_t}^{p_s} \hat{S}_q dp = -\int dA \int_{p_t}^{p_s} C dp - \int (\omega q')|_{p=p_s} dA. \tag{10}$$

For a cloud known not to be precipitating, storing or exporting condensed water, the first term on the right side of (10) must be zero. This leads to a zero integrated value of $\hat{S}_q$ if the surface latent heat flux is zero. Conversely, if the surface flux is known to be negligible, the integrated value of $\hat{S}_q$ is minus the net condensation rate in the cloud.

3. Observations

The observations described in this paper were conducted over the Langmuir Laboratory for Atmospheric Research. Langmuir Laboratory sits atop the Magdalena Mountains of west-central New Mexico. This forested range is aligned north–south, and is about 20 km long by 10 km wide. It is surrounded by grasslands and low scrub of predominant elevation 1800 m on the east side and 2100 m on the west. The highest elevation in the Magdalena Mountains is about 3200 m. A topographic map of the mountains and adjacent area is shown by Raymond and Wilkening (1982).

Fifteen flights were made by the NCAR Sabreliner from 9 to 27 August 1982. Table 1 shows the dates of these flights, the conditions encountered and the

TABLE 1. Summary of flight operations during August 1982.

Flight	Date (August 1982)	Conditions and operations
1	9	No moist convection; test maneuvers only
2	10	Cumulus congestus over Magdalena Mountains; boxes
3	11	Cumulus congestus over Magdalena Mountains; boxes
4	12	Rain shower starts over Magdalena Mountains, drifts north; boxes
5	13	Rain shower starts over Magdalena Mountains, drifts north; boxes
6	14	Stratus deck, chaotic conditions; no analysis
7	16	Rain shower over Magdalena Mountains; boxes
8	18	Data system failure
9	19	Thunderstorm over Magdalena Mountains, centimeter-size hail; boxes
10	20	Thunderstorm northwest of Magdalena Mountains, drifts west; boxes
11	21	Cumulus congestus, transient light rain over Magdalena Mountains; boxes
12	24	Rain shower over Magdalena Mountains, neighboring storm interferes; boxes
13	25	North–south line of thunderstorms northwest of Magdalena Mountains, tornado; boxes
14	26	Cumulus congestus over Magdalena Mountains, neighboring storm interferes; boxes
15	27	Cumulus congestus; test maneuvers only

operations undertaken. Times in the table and throughout the paper are Mountain Daylight Time (MDT), or GMT − 6 h. The Sabreliner was based at Albuquerque, approximately 120 km north-northeast of Langmuir Laboratory. Visibility was usually such that clouds over Langmuir Laboratory could be seen from Albuquerque. The Sabreliner typically launched when the clouds were observed to reach towering cumulus or congestus stage.

A fast-scanning 3 cm radar (Krehbiel and Brook, 1979) was based at Langmuir Laboratory during the aircraft operations. Radio contact between the radar and the aircraft made radar echo information available in real time.

Time-lapse movies of clouds over Langmuir Laboratory were made from Socorro (26 km east-northeast) during the observational period as well.

The accuracy of detrained mass flux observations made by aircraft is marginal for storms of the type observed here. Raymond and Wilkening (1982) analyzed the accuracy of this type of observation made with the NCAR Queen Air. All the same factors apply here with the exception that the Sabreliner, due to its greater speed, makes steeper banks during turns. Thus, inaccuracies induced by turning need to be seriously considered. These matters are taken up in the Appendix. The resulting estimate for the uncertainty in the detrained mass flux measurement is roughly ± 0.02 km^2 s^{-1} for boxes of 80 km circumference.

The winds were from the south at all levels during most of the observational period. Winds from this direction result in little or no convective development upwind of Langmuir Laboratory. However, when the wind shifts to a more westerly direction, storms forming over the neighboring San Mateo Mountains often interfere with and engulf the Magdalena Mountain storms.

The persistent southerly flow during the summer of 1982 caused some incipient thunderstorms to blow off the mountain and decay during the observational period. On a number of occasions we studied thunderstorms that formed near, but not over the Magdalena Mountains.

Detrained fluxes of mass F, moisture F_q, potential temperature F_θ, and equivalent potential temperature F_e were computed for all box maneuvers in flights 2, 3, 4, 5, 7, 9, 10, 11, and 13. Flights 12 and 14 were excluded due to the presence of an interfering storm, while flights 1 and 15 were test flights only. No suitable convection occurred on flight 6, and a data system problem occurred on flight 8. This data set thus includes all usable data obtained during the program, and is shown in Table 2. The translation velocity $\mathbf{V}_t$ for each system was estimated from the displacement of successive box maneuvers. Some systems tended to remain in place over their point of origin, whereas others appeared in drift. In some cases an abrupt change in translational velocity occurred, generally coincident with the onset of precipitation. These changes are reflected in Table 2.

4. Results

The data were stratified by the intensity of the observed convection. The cumulus congestus data set includes all boxes from flights 2, 3 and 11. None of these systems evolved into a thunderstorm, though the flight 11 case produced a slight amount of rain. Boxes 1–5 of flight 9, 1–7 of flight 10 and 1–4 of flight 13 were taken as representative of the mature phase of active thunderstorms. Flights 4, 5 and 7 observed weaker precipitating systems and are not analyzed further.

Figures 1 and 2 respectively show composited thermodynamic profiles for the congestus and thunderstorm cases, obtained from box maneuver averages. Potential temperature and low-level moisture profiles are virtually identical for the two cases. The only significant difference is the midlevel moisture—the 550 mb mixing ratio for the thunderstorm composite exceeds the congestus case by more than a factor of 2. This suggests that drying out of clouds by midlevel entrainment is a significant inhibiting factor in the development of thunderstorms under these conditions.

Figure 3 shows the composited soundings for both cases plotted on a skew-T chart. The differences in midlevel moisture show up dramatically in this presentation.

It is clear from Fig. 3 that even when thunderstorms did occur, they were energetically marginal. In particular, the only air capable of rising buoyantly to anvil levels is that originating very near the surface. Dilution with even a small amount of air from higher than 700 mb would prevent this from happening.

Figures 4 and 5 show the composited westerly and southerly wind components for the congestus and thunderstorm cases. The winds are generally light in both cases. The large scatter precludes drawing significant mean profiles.

Figures 6 and 7 respectively show composited profiles of detrained mass flux F for the congestus and thunderstorm cases. In each case the solid line on the graph is a subjective fit to the data. The dashed line has a constant offset added to make the vertical mass flux zero at high levels. In both cases the offset is within the expected systematic error for our measurement of F. The dashed-line data are used for further analysis. The thunderstorm case is rather data-sparse at upper levels, so the drawn profile above 500 mb should be considered qualitative.

The thunderstorm results are quite similar to those obtained by many other observers from the Thunderstorm Project (Braham, 1952) onward (Fankhauser, 1969, 1974; Betts, 1973; McNab and Betts, 1978). The congestus results appear to be new.

TABLE 2. Summary of all useful boxes during 1982 project. Time is MDT = GMT − 6 h. Pressure p is in mb. Detrained mass flux F is in km^2 s^{-1}. Detrained moisture flux F_q is in g kg^{-1} · km^2 s^{-1}. Detrained potential and equivalent potential temperatures are in K km^2 s^{-1}. Storm translational velocity V_t is resolved into westerly and southerly components with units of m s^{-1}.

Flight	Box	p (mb)	Time (MDT)	F	F	F_q	F_e	V_t	Comment
2	1	770	1101	−0.086	0.060	−0.049	−0.075	0, 0	Small cumulus at 1150
	2	467	1131	−0.015	−0.024	0.010	0.010		
	3	650	1145	−0.004	−0.018	0.131	0.359		Tops 500 mb
	4	703	1156	−0.022	−0.010	0.157	0.442		
	5	760	1208	−0.026	0.056	−0.009	0.037		No rain
3	1	547	1149	−0.014	−0.036	0.025	0.041	0, 0	Congestus
	2	707	1205	−0.018	0.015	0.003	0.027		
	3	735	1215	−0.042	0.033	0.011	0.070		
	4	763	1228	−0.105	0.027	0.000	0.030		
	5	736	1239	−0.063	0.022	0.003	0.034		
	6	707	1250	−0.040	0.019	0.003	0.029		
4	1	469	1154	0.020	−0.054	0.009	−0.023	0, 0	No echo
	2	378	1200	−0.015	0.034	−0.025	−0.052		Aircraft well above top
	3	670	1212	0.001	−0.025	0.015	0.017		
	4	706	1218	−0.030	−0.005	0.001	−0.004		Precipitation observed
	5	466	1226	−0.010	0.026	0.007	0.049	−0.6, 6.9	
	6	411	1233	−0.022	−0.025	−0.003	−0.036		Aircraft at cloud top
	7	377	1240	−0.001	0.003	0.003	0.013		Precipitation, no anvil cloud
5	1	449	1142	−0.006	0.086	0.006	0.106	0, 0	Aircraft just below top
	2	449	1149	−0.002	0.111	0.000	0.115		Tops now 370 mb
	3	449	1156	−0.005	0.097	−0.001	0.096		
	4	449	1203	−0.003	0.054	0.004	0.067	2.8, 5.0	
	5	487	1217	0.026	0.074	0.013	0.117		First echo
	6	535	1228	−0.043	−0.041	0.059	0.133		
	7	581	1241	−0.039	0.001	0.027	0.080		Precipitation observed
	8	629	1256	0.000	0.027	0.030	0.056		
7	1	454	1250	0.002	−0.027	0.089	0.256	0, 0	Rain shaft and anvil
	2	393	1300	−0.030	0.001	0.003	0.013		Rain on NE side
	3	376	1309	−0.020	−0.026	0.020	0.040		
	4	360	1316	0.039	0.002	0.040	0.136		Through anvil
	5	345	1325	0.053	0.006	0.051	0.183		Storm dissipating on radar
	6	329	1334	0.020	−0.030	0.019	0.035		
	7	759	1352	−0.071	−0.022	0.029	0.060		Towering cumulus over Magdalenas
9	1	373	1359	−0.035	−0.014	0.016	0.041	0, 0	Vigorous thunderstorm
	2	314	1409	−0.017	−0.140	0.008	−0.114		Lightning hits radar
	3	259	1419	0.085	0.130	0.026	0.223		Aircraft just below tops
	4	465	1430	0.096	−0.025	−0.002	−0.033		
	5	554	1441	−0.023	−0.020	0.025	0.053		Storm weakening
	6	664	1453	−0.029	0.007	−0.012	−0.027		Just light rain
	7	760	1505	−0.009	−0.016	0.035	0.084		
10	1	762	1251	−0.059	0.004	0.023	0.073	−2.2, 1.1	Vigorous thunderstorm
	2	697	1302	−0.007	0.004	0.006	0.022		NW of Magdalenas
	3	645	1311	−0.032	−0.007	0.011	0.024		
	4	549	1320	−0.032	0.000	0.030	0.090		
	5	464	1329	0.009	−0.018	0.002	−0.013		
	6	408	1339	−0.010	−0.053	0.048	0.100		
	7	341	1352	−0.010	−0.021	0.035	0.098		
11	1	765	1351	−0.083	−0.020	0.010	0.006	0, 0	Bases ragged, congestus
	2	654	1403	0.051	0.018	0.083	0.260		Echo
	3	558	1414	0.011	−0.030	0.103	0.282		Echo dissipates, light rain
	4	463	1424	0.006	−0.001	0.007	0.022		Congestus
13	1	595	1545	−0.045	0.000	0.011	0.029	−0.5, 0.9	Line of vigorous thunderstorms
	2	630	1554	−0.049	−0.064	0.037	0.038		
	3	685	1602	−0.031	0.056	−0.112	−0.259		
	4	736	1613	−0.026	0.007	−0.014	−0.034		Tornado on nearby storm
	5	783	1622	0.003	−0.018	−0.002	−0.027		Storm dissipating

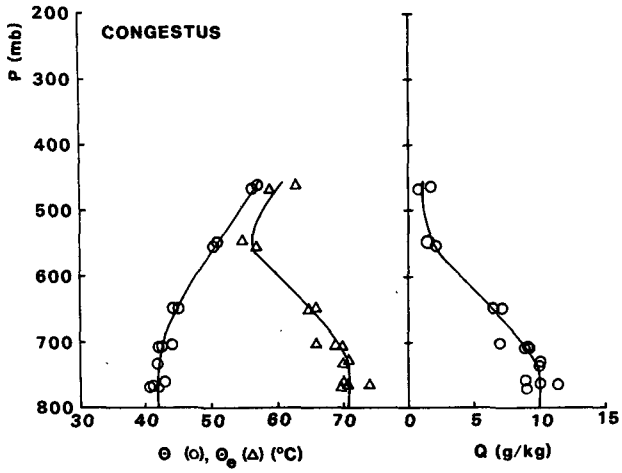

FIG. 1. Composite thermodynamic sounding for the cumulus congestus case. The data points are average values for box maneuvers on flights 2, 3 and 11, while the lines are subjective analyses.

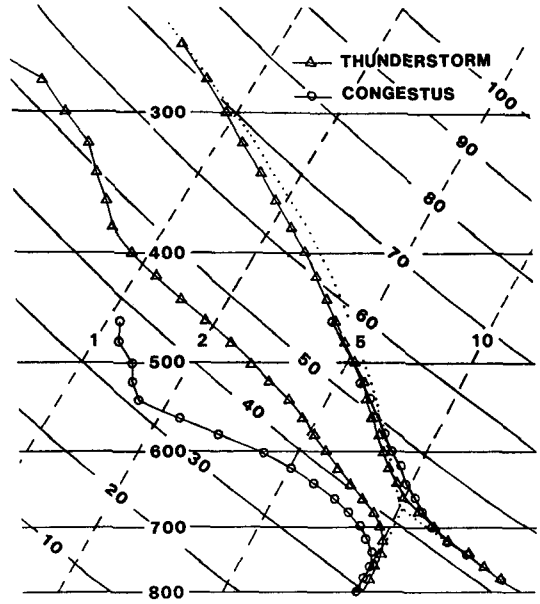

FIG. 3. Skew-T chart representation of the thermodynamic soundings shown in Figs. 1 and 2. The pressure p is in mb while the potential temperature is in °C. The dashed lines representing mixing ratio are given in units of g kg^{-1}. The dotted line is the moist adiabat for boundary layer air.

The differences between the congestus and thunderstorm detrained mass flux profiles are quite dramatic. In particular, while the thunderstorms have net mass influx up to 500 mb, the congestus clouds appear to detrain air above 700 mb. In fact, much of the detrainment occurs below cloud base, which is typically 630 mb for these clouds. The case for strong subcloud detrainment in congestus clouds is supported by the earlier results of Raymond and Wilkening (1982), which were heavily weighted toward nonprecipitating systems.

The detrainment layer near 470 mb in the thunderstorm case is represented by only one point in Fig. 7. However, visual evidence for such detrainment is often (but not invariably) seen in the form of shelves of stratus protruding from the sides of New Mexico thunderstorms. Furthermore, two cases of such midlevel detrainment were documented in our previous study (Raymond and Wilkening, 1982).

Figure 8 shows the vertical mass flux $\hat{\omega}$, obtained by integrating the curves in Figs. 6 and 7 using (6). Given the uncertain nature of the detrained mass fluxes, these profiles must be considered qualitative. However, certain conclusions are still warranted. In particular, it is clear that the congestus vertical mass flux peaks near mountain-top level, or well below cloud base. This suggests that these congestus clouds

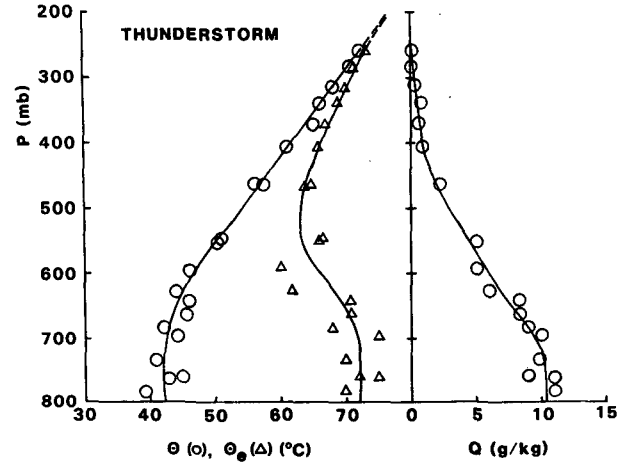

FIG. 2. As in Fig. 1 except the thunderstorm composite, consisting of flights 9, 10 and 13.

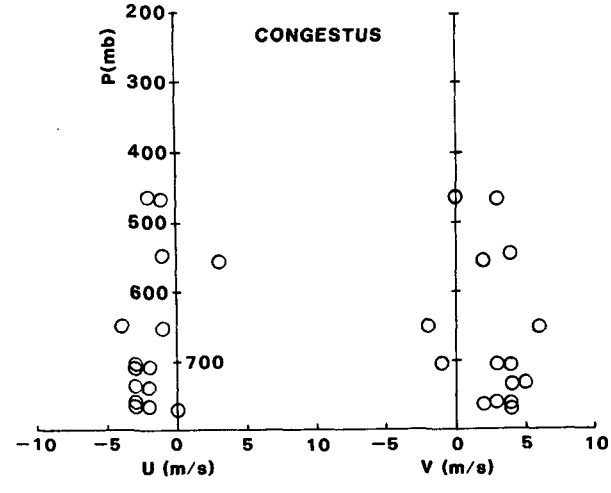

FIG. 4. Composited U (westerly) and V (southerly) wind components for the congestus case. No analysis was attempted due to the scatter of the points.

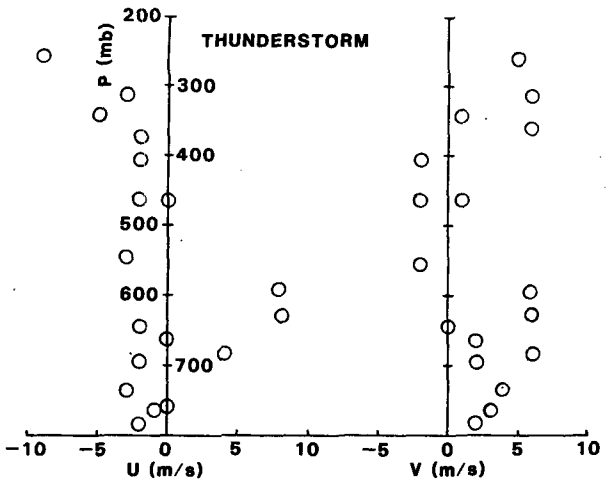

FIG. 5. As in Fig. 4 except the thunderstorm composite.

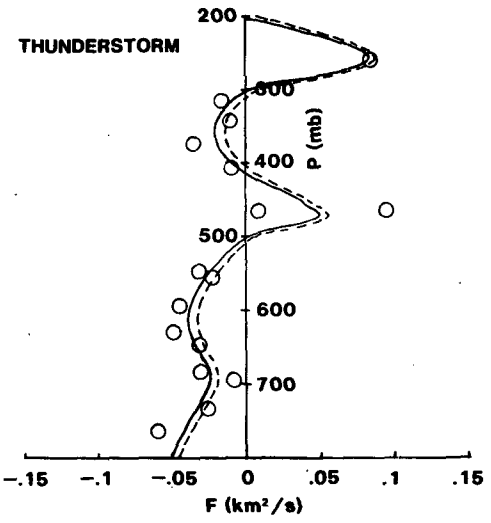

FIG. 7. As in Fig. 6 except for the thunderstorm case.

are merely moist extensions of the planetary boundary layer, even though they have tops higher than 500 mb. The thunderstorms, on the other hand, have a bimodal structure with the peak vertical mass flux at a much greater elevation. This bimodal structure is also seen in the results of Fankhauser (1969) and McNab and Betts (1978) and is related to the midlevel detrainment.

Figures 9–11 show the composited detrained fluxes of water vapor mixing ratio, potential temperature and equivalent potential temperature for the congestus case, while Figs. 12–14 show equivalent results for the thunderstorms. The lines are again subjective fits to the data. Congestus clouds tend to detrain large quantities of water vapor between 550 and 700 mb, while thunderstorms detrain very little. The amount of water detrained from thunderstorms in the form of ice crystals leaving the anvil was unfortunately not measured.

Potential temperature detrainment from a cloud should be small if the measurement is made far enough from the cloud because detrained parcels tend to seek their level of neutral buoyancy, which in the absence of virtual temperature effects implies zero potential temperature anomaly in detrained air.

Both congestus clouds and thunderstorms show some detrained potential temperature flux, as shown by Figs. 10 and 13. With the exception of a few anomalous cases, both congestus clouds and thunderstorms tend to heat lower levels and cool upper levels via these terms, with the heating being more pronounced in the congestus case.

The total effect of clouds on the atmosphere is

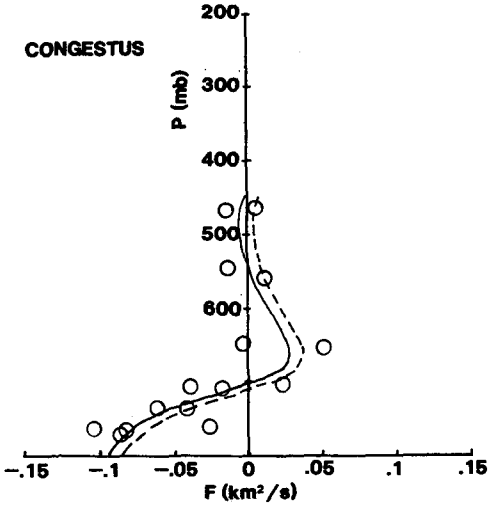

FIG. 6. Detrained mass flux for the congestus case. The solid line is a subjectively analyzed curve. The dashed line has a constant correction added to make the vertical mass flux zero at cloud top.

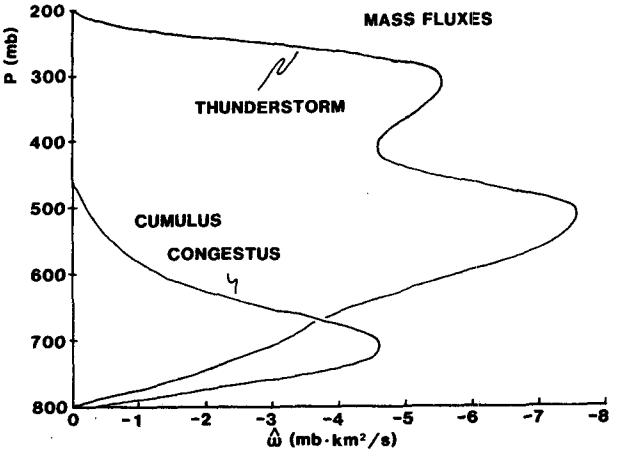

FIG. 8. Vertical mass fluxes for the congestus and thunderstorm cases, obtained by integrating the curves to Figs. 6 and 7.

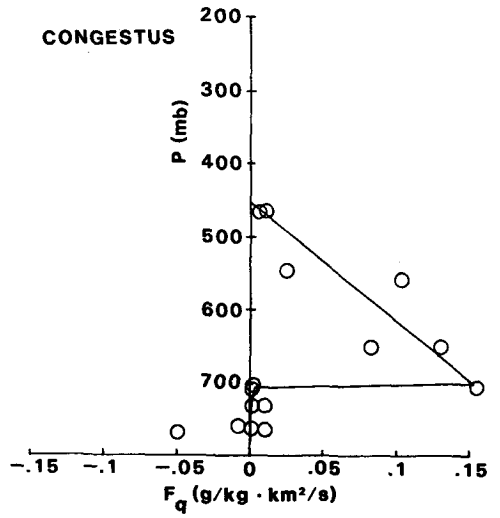

FIG. 9. Composite of detrained moisture flux for the congestus case. The line is a subjective analysis of the data.

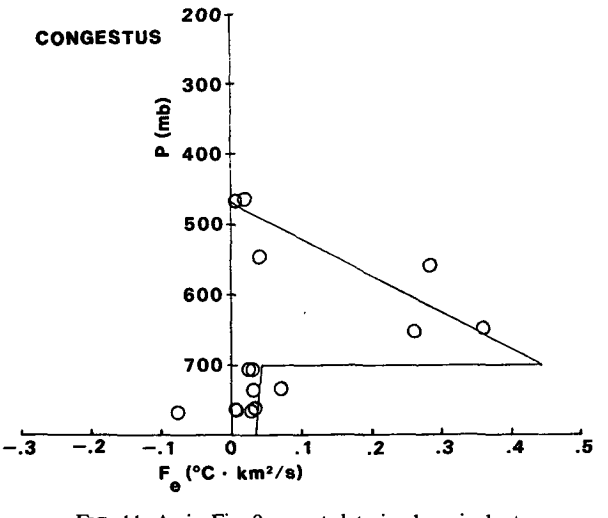

FIG. 11. As in Fig. 9 except detrained equivalent potential temperature flux.

given by the apparent sources of moisture, potential temperature and equivalent potential temperature.

As (4) shows, the apparent source of a variable depends on the detrained flux of that variable, the vertical mass flux and the time rate of change of that variable integrated over the cloud area. We have computed the apparent sources of potential temperature, moisture and equivalent potential temperature for the congestus and thunderstorm composites on the assumption that the time derivative term can be neglected (Figs. 15–17). This is probably valid for the congestus cases, which appeared to be in a nearly steady state. It is probably also valid for the potential temperature in the thunderstorm case, as buoyancy forces tend to keep a large potential temperature anomaly from forming within a cloud. Thus, only the moisture and equivalent potential temperature sources for the thunderstorm composite are likely to be subject to a large error from this cause. Errors of this type were discussed by McNab and Betts (1978).

Additional errors are introduced by the approximate nature of the computed $\hat{\omega}$ profiles. This needs to be kept in mind when interpreting the results of the computations.

The primary effect of congestus clouds is to dry the subcloud layer ($p > 640$ mb) and moisten the cloud layer (460 mb $< p <$ 640 mb). The atmosphere below 580 mb is also warmed, with a peak near 690 mb. Slight cooling may occur above 580 mb. A tendency to increase θ_e in the cloud layer is accom-

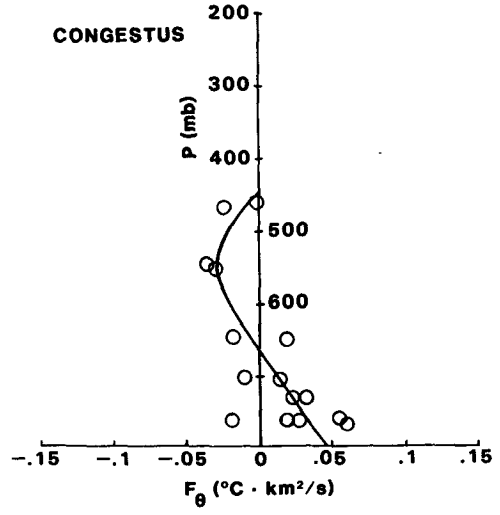

FIG. 10. As in Fig. 9 except detrained potential temperature flux.

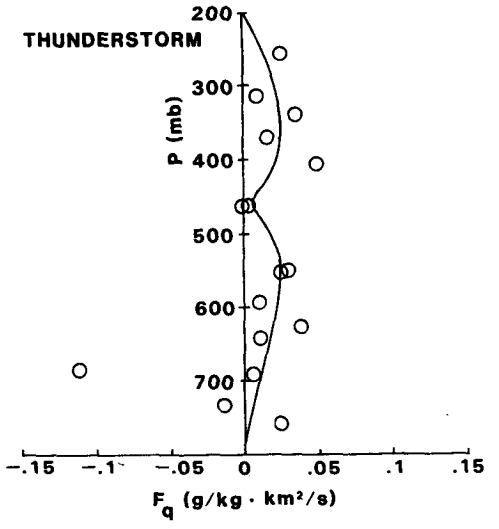

FIG. 12. As in Fig. 9 except detrained moisture flux, thunderstorm case.

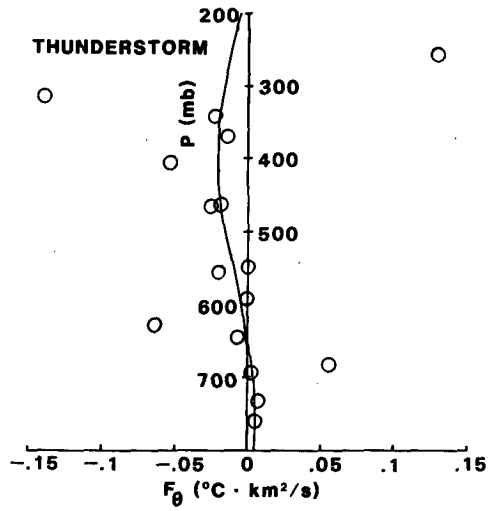

FIG. 13. As in Fig. 12 except detrained potential temperature flux.

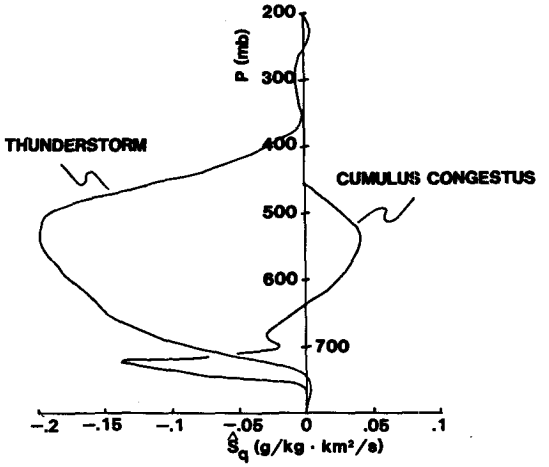

FIG. 15. Computed apparent moisture source for cumulus congestus and thunderstorm cases.

panied by a tendency to decrease it below 700 mb.

To the extent that we can believe the thunderstorm data, it appears that thunderstorms dry a deep layer from near the surface to about 400 mb. Warming is induced from cloud base to cloud top and is centered at a somewhat higher level than the drying. This agrees with the results of Yanai *et al.* (1973) on tropical oceanic clouds. The double peak in the heating is related to the similar structure in the vertical mass flux. Thunderstorms tend to increase θ_e at high levels and decrease it at low levels.

The pressure-integrated value of $\hat{S}_q$ is -1 mb g kg^{-1} km^2 s^{-1} for the congestus case and -46 for the thunderstorm case. In essence, the positive and negative parts of S_q cancel in the integral in the congestus case, which is consistent with negligible surface latent heat flux and precipitation inside the observational box.

Assuming that negligible condensed water is lost via ice detrainment from the anvil, the thunderstorm figure corresponds to an areally integrated precipitation rate of 4.7×10^5 kg s^{-1}. This is equivalent to 17 mm h^{-1} over a 100 km^2 area.

The equivalent potential temperature flux obtained by integrating $\hat{S}_e$ in pressure is shown for both the congestus and thunderstorm cases in Fig. 18. The heat flux scale is derived using the normalization expressed in (9) with $\langle\theta_e\rangle$ = 340 K, $\langle T\rangle$ = 270 K, and an assumed area of 357 km^2, which was the average area inside a box for the project.

The nearly monotonic decrease of θ_e flux with height for the congestus case is further evidence that the observed cumulus congestus clouds are totally

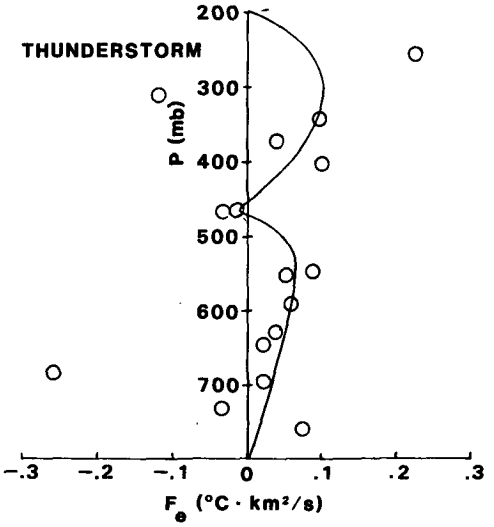

FIG. 14. As in Fig. 12 except detrained equivalent potential temperature flux.

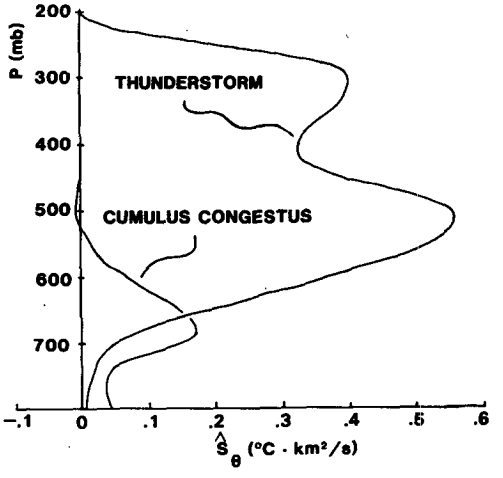

FIG. 16. As in Fig. 15 except computed apparent source of potential temperature.

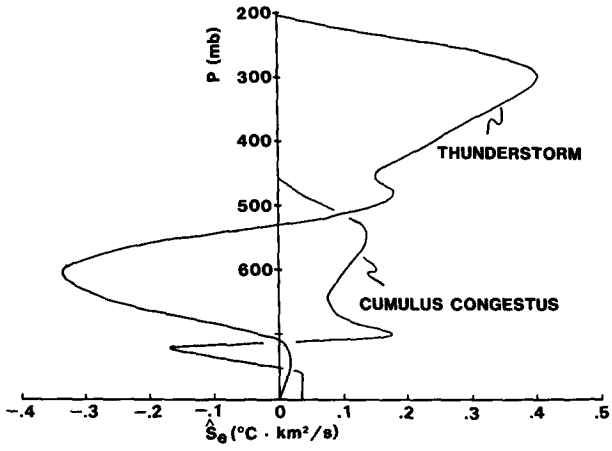

FIG. 17. As in Fig. 15 except for equivalent potential temperature.

dependent on boundary layer forcing. The derived surface heat flux of 500 W m^{-2} is slightly higher than, but of the same order of magnitude as, that derived by Raymond and Wilkening (1982) by an independent method.

The larger (1000 W m^{-2}) surface heat flux associated with thunderstorms is implausible. If anything, reduced insolation due to greater cloud coverage should make the surface heat flux less. (See McNab and Betts, 1978.) We see three possible explanations for this anomaly:

1) The $\hat{S}_e$ profile is very dependent upon the structure of the vertical mass flux at upper levels. As previously mentioned, this is the most uncertain facet of our data, and errors here could translate into an excessive derived surface heat flux.

2) It is possible that significant cold outflows occurred below the minimum flight level of the aircraft. This corresponds to a net influx of moist static energy at low levels, which in the present analysis would be mistaken for a surface heat flux.

3) A negative $\partial\theta_e/\partial t$ averaged over the cloud would have acted to decrease the average value of $\hat{S}_e$, resulting in a smaller surface heat flux.

Clearly, this matter requires further investigation.

5. Interpretation

The observation that thunderstorms have net inflow up to roughly 500 mb is not new, but the marginal instability exhibited by our cases allows us to rule out a common interpretation of this result. The observed inflow structure is sometimes taken as evidence in support of the entraining plume model of a thunderstorm. However, the ambient air above 700 mb cannot be a significant updraft component—its equivalent potential temperature is simply too low.

The alternate interpretation, expressed by Betts (1973) and others, is that air entering the storm between the top of the boundary layer and the level of nondivergence feeds the downdraft. The updraft then consists of air originating below 700 mb and ascending essentially unmixed.

Support for this interpretation comes from the vertical mass flux profile in the cumulus congestus case—these clouds indeed appear to draw their updrafts from below 700 mb.

It is interesting to note that the peak vertical mass flux for the thunderstorm composite is only slightly greater than that for the congestus case (see Fig. 8). This would seem to rule out significant positive feedback between latent heat release and generation of low-level convergence, as apparently occurs in squall lines and other large convective systems. Such feedback would presumably result in considerable intensification of the thunderstorm circulation over the congestus and dry cases, which is not observed. The evidence thus indicates that the only difference between the cumulus congestus and thunderstorm cases is that convective elements ascend to higher elevations and make more precipitation in the thunderstorms. The low-level forcing, which is responsible for determining the updraft mass flux, appears to be about the same in the two cases.

If the above conclusion is correct, the difference between the thunderstorm and congestus mass fluxes at low levels must be ascribed to the thunderstorm downdraft. In fact, the net vertical mass flux at 700 mb in the thunderstorm cases is only one-half of the corresponding congestus flux. This suggests that the thunderstorm downdraft strength at 700 mb averages about one-half of the updraft strength in the storms we measured.

The vertical mass flux in the congestus composite becomes small well below cloud top. However, as a comparison of Figs. 8 and 9 shows, significant mois-

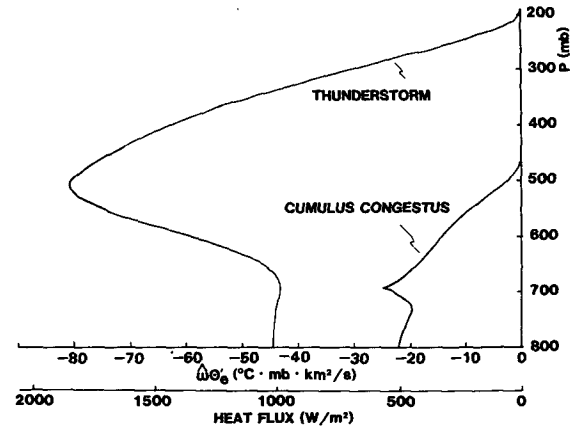

FIG. 18. Vertical flux of equivalent potential temperature for congestus and thunderstorm composites. These curves are obtained by integrating the curves of Fig. 17 in pressure, assuming negligible effects from radiation.

ture is being transported to heights in these clouds well above the cutoff in vertical mass flux, implying that updrafts exist above this level but are counterbalanced by downdrafts. Thus, no net upward transfer of mass takes place there but only eddy transfer of energy and moisture.

The above observation supports the vertical mixing model of nonprecipitating cumulus clouds in which downdrafts are driven by evaporation of cloud matter in dry, midlevel air. (See Telford, 1975; Paluch, 1979; Raymond, 1979; Emanuel, 1981.)

Previous observations by Raymond and Wilkening (1982) suggest that the midlevel detrainment observed in some thunderstorms and cumulus congestus clouds is also driven by vertical mixing. The most convincing evidence for this is a time-lapse movie taken during the 1980 program showing convective towers collapsing and spreading out into a midlevel stratus layer.

Figure 7 shows weak inflow in the thunderstorm case between 300 and 400 mb. We speculate that this inflow mixes with updraft air to produce the observed midlevel outflow. The originating level for this inflow is roughly consistent with the observed cloud top in the time-lapse movie.

Figure 19 summarizes the above arguments about cumulus congestus and thunderstorm mass fluxes. In the congestus case, curve A represents the updraft mass flux, which transports air from below 700 mb to near cloud top, and curve B the downdraft mass flux resulting from evaporation at cloud top. The strength and penetration depth of the downdraft is adjusted to make the net mass flux (curve D) agree with Fig. 8.

For the thunderstorm case the updraft (curve A) takes air from below 700 mb to anvil level at 200–300 mb. Consistent with the height of the midlevel detrainment, part of the updraft is lost between 400 and 500 mb to mixing with dry air originating above 400 mb (curve B). Finally, the precipitation-induced downdraft (curve C) is adjusted to make the composite mass flux (curve D) look like Fig. 8.

We hope that the preceding construct stimulates theoretical work on the structure of convective clouds. In particular, we recognize a number of intriguing questions:

1) What determines whether convective elements produced in the boundary layer will stop at middle levels or reach thunderstorm heights in situations of marginal instability?

2) Why do the hypothesized, mixing-induced downdrafts draw their dry air from different levels in the congestus and thunderstorm cases?

3) Why does detrainment occur below 600 mb and above 500 mb, but not in between?

4) How can parcels remain essentially unmixed through many kilometers of vertical displacement in such a turbulent entity as a cumulus cloud?

5) Why does mixing then take place where it does?

Acknowledgments. Many people contributed to the success of this program. The staff of NCAR's Research Aviation Facility not only made the Sabreliner fly, but also made it yield useful data. Paul Krehbiel was responsible for the operation of the radar at Langmuir Laboratory. Julie Rohwein flew as an observer on the Sabreliner and analyzed much of the data. Mark Duggins and Dale Harris drew the figures, and Debbie Brook typed the manuscript. The comments by Richard Rotunno and two reviewers resulted in substantial clarification of the original manuscript. This work was supported by National Science Foundation Grants ATM-81-08693 and ATM-83-11017.

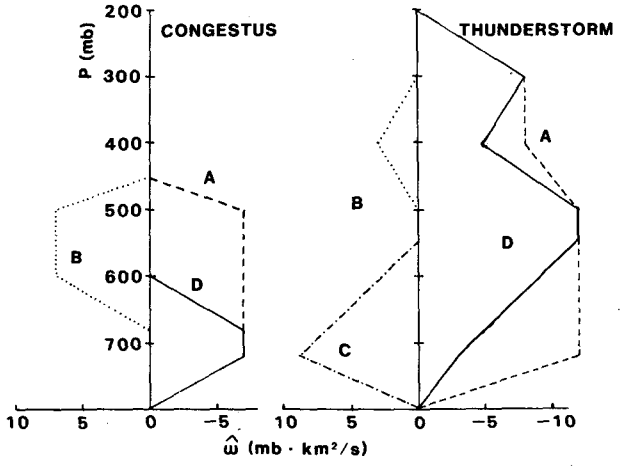

FIG. 19. Hypothesized model for various components of the mass flux in the congestus and thunderstorm composites. (a) Updraft mass flux; (b) downdraft induced by vertical mixing and evaporation of cloud droplets; (c) downdraft induced by precipitation; (d) net mass flux, to be compared with Fig. 8.

APPENDIX

Uncertainty in the Detrained Mass Flux Measurement

The detrained mass flux F is given by

$$F = \oint (\mathbf{v}_r + \mathbf{v}_a) \cdot \mathbf{n} dl, \qquad \text{(A1)}$$

where $\mathbf{v}_r$ is the wind relative to the aircraft, $\mathbf{v}_a$ is the aircraft velocity, and $\mathbf{n}$ is the unit normal to the aircraft track pointing horizontally outward. The surface-relative wind $\mathbf{v} = \mathbf{v}_r + \mathbf{v}_a$, so (A1) is equivalent to (6).

Raymond and Wilkening (1982) discussed errors in F induced by the 84 min inertial platform oscillation. These errors go as the square of the time to complete a box, and are of the order 0.01 km^2 s^{-1} for a 20 min Queen Air box. Sabreliner boxes took 10 min or less during the 1982 project, which reduces this uncertainty to approximately 0.002 km^2 s^{-1}, a negligible value.

The primary errors induced by the Sabreliner come from uncertainties in the component of $\mathbf{v}_r$ normal to the flight path, or to good approximation in light winds, the component normal to aircraft heading.

For small values of the angle of attack α and the slip angle β, the component of $\mathbf{v}$ normal to the aircraft heading is

$$v_n = v_{an} + v_{rn} = v_{an} - U_a(\beta \cos\phi - \alpha \sin\phi), \quad \text{(A2)}$$

where U_a is the aircraft true airspeed and ϕ is the roll angle. The angle of attack becomes involved in the wind calculation when the aircraft turns.

The vast majority of the Sabreliner operations were conducted at less than Mach 0.5. Incompressible gas dynamics are therefore used to derive angle of attack and slip angle:

$$\alpha = A + C\Delta p_\alpha / p_d, \quad \text{(A3)}$$

$$\beta = B + D\Delta p_\beta / p_d. \quad \text{(A4)}$$

The vertical differential pressure from the gust probe is Δp_α, while Δp_β is the horizontal differential pressure. The pitot minus static, or dynamic pressure, is given by p_d. Assuming zero vertical wind, pitch maneuvers and speed change maneuvers can be used to derive A and C. A fit of (A3) to a set of these maneuvers yields $A = 0.0101$ and $C = 0.2250$ where α is measured in radians. Yaw maneuvers yield $D = 0.2321$, where β is also measured in radians.

The B cannot be determined from yaw maneuvers due to the unknown horizontal wind. However, (A2) can be rearranged to yield

$$BU_a \cos\phi + U\cos\psi - V\sin\psi = v_{an} - U_a(\beta' \cos\phi - \alpha \sin\phi), \quad \text{(A5)}$$

where ψ is the heading angle of the aircraft and U and V are the Cartesian components of the wind. The last two terms on the left side of (A5) combine to form v_{rn}, and the slip angle has been split into B and $\beta' = D\Delta p_\beta / p_d$. [See (A4).]

Everything on the right side of (A5) is known. Assuming U and V to be unknown constants over a reverse heading maneuver allows a fit to be made for B, U and V. We obtain $B = 0.00925$ as an average over many reverse heading maneuvers.

With the attack and slip angle calibrations thus obtained, the wind can be computed in the conventional manner (Lenschow, 1981). As a test of the calibrations, steeply banked left and right turns at the minimum and maximum speeds of the Sabreliner were flow in clear air. The detrained mass flux should be zero for these small boxes. The result is an rms value of 0.006 km^2 s^{-1}.

This exercise tests the angle of attack calibrations, but is relatively insensitive to errors in B, the slip offset. However, the variance in the reverse track determinations of B suggests an uncertainty in B of roughly 1.4×10^{-3} radians. For an 80 km box track flown at 150 m s^{-1}, this is equivalent to an uncertainty in F of ± 0.017 km^2 s^{-1}. This suggests a total uncertainty due to combined slip angle and attack angle errors of roughly ± 0.02 km^2 s^{-1} for the typical box flown in this project.

There has been some concern expressed that the Sabreliner gust probe boom bends in response to aerodynamic loading. However, all boxes were flown at approximately the same indicated airspeed. This implies a constant dynamic pressure, and hence a uniform aerodynamic bending if this indeed takes place. The effects of such a constant offset would have been removed by the calibration procedure.

NCAR's attack and slip angle calibration procedure is designed to operate over a broad range of dynamic pressure and Mach number. For the limited range of these parameters encountered during our observations, we believe that our calibration is slightly more accurate.

REFERENCES

Betts, A. K., 1973: A composite mesoscale cumulonimbus budget. *J. Atmos. Sci.*, **30,** 597–610.

Braham, R. R., 1952: The water and energy budgets of the thunderstorm and their relation to thunderstorm development. *J. Meteor.*, **9,** 227–242.

Emanuel, K. A., 1981: A similarity theory for unsaturated downdrafts within clouds. *J. Atmos. Sci.*, **38,** 1541–1557.

Fankhauser, J. C., 1969: Convective processes resolved by a mesoscale rawinsonde network. *J. Appl. Meteor.*, **8,** 778–798.

——, 1974: The derivation of consistent fields of wind and geopotential height from mesoscale rawinsonde data. *J. Appl. Meteor.*, **13,** 637–646.

Krehbiel, P. R., and M. Brook, 1979: A broad-based noise technique for fast-scanning radar observations of clouds and clutter targets. *IEEE Trans. Geosci. Electron.*, **GE-17,** 196–204.

Lenschow, D. H., 1981: The measurement of air velocity and temperature using the NCAR Buffalo aircraft measuring system. Revised edition, NCAR-TN/EDD-74. [Available from the National Center for Atmospheric Research, Box 3000, Boulder, CO.]

McNab, A. L., and A. K. Betts, 1978: A mesoscale budget study of cumulus convection. *Mon. Wea. Rev.*, **106,** 1317–1331.

Ogura, Y., and L. Chen, 1977: A life history of an intense mesoscale convective storm in Oklahoma. *J. Atmos. Sci.*, **34,** 1458–1476.

Paluch, I. R., 1979: The entrainment mechanism in Colorado cumuli. *J. Atmos. Sci.*, **36,** 2467–2478.

Raymond, D. J., 1979: A two-scale model of moist, nonprecipitating convection. *J. Atmos. Sci.*, **36,** 816–831.

——, and M. Wilkening, 1980: Mountain-induced convection under fair weather conditions. *J. Atmos. Sci.*, **37,** 2693–2706.

——, and ——, 1982: Flow and mixing in New Mexico mountain cumuli. *J. Atmos. Sci.*, **39,** 2211–2228.

Sanders, F., and R. J. Paine, 1975: The structure and thermodynamics of an intense mesoscale convective storm in Oklahoma. *J. Atmos. Sci.*, **32,** 1563–1579.

Telford, J. W., 1975: Turbulence, entrainment, and mixing in cloud dynamics. *Pure Appl. Geophys.*, **113,** 1067–1084.

Yanai, M., S. Esbensen and J. H. Chu, 1973: Determination of bulk properties of tropical cloud clusters from large scale heat and moisture budgets. *J. Atmos. Sci.*, **30,** 611–627.